PHYSICAL REVIEW E **72**, 026407 (2005)

Characterization and control of plasma density distribution for the development of solid-target x-ray lasers

M.-C. Chou,[1,2] P.-H. Lin,[1] H.-E. Tsai,[1,3] D.-L. Chen,[1] C.-H. Lee,[4] J.-Y. Lin,[2] J. Wang,[1,3] and S.-Y. Chen[1,5]
[1]*Institute of Atomic and Molecular Sciences, Academia Sinica, Taipei 106, Taiwan*
[2]*Department of Physics, National Chung Cheng University, Chia-Yi 621, Taiwan*
[3]*Graduate Institute of Electro-Optical Engineering, National Taiwan University, Taipei 106, Taiwan*
[4]*Research Center for Applied Science, Academia Sinica, Taipei 115, Taiwan*
[5]*Department of Physics, National Central University, Jung-Li 320, Taiwan*
(Received 23 March 2005; published 15 August 2005)

By using deflectometry of a longitudinal probe pulse and reflective interferometry of a transverse probe pulse to resolve the spatiotemporal distribution of the preformed plasma, we characterize and control the plasma density distribution near the target surface for the development of solid-target x-ray lasers. We show that the use of prepulses in an ignitor-heater scheme can increase the scale length of the preformed plasma and how the effect varies with target materials. Many important issues crucial to x-ray lasing such as electron density distribution, electron temperature, and the optimal timing between pumping pulses can be resolved with these methods.

DOI: 10.1103/PhysRevE.72.026407 PACS number(s): 52.50.Jm, 52.70.Kz, 42.55.Vc

I. INTRODUCTION

Since a soft x-ray laser was conclusively demonstrated with Ne-like Se at 20.6 and 20.9 nm in 1985 [1,2], the development of x-ray laser has been intensively pursued for its promise in providing an ultrashort high-intensity coherent x-ray source for important applications in medicine, biology, chemistry, and physics. Significant progress has been made in the past few years to push the x-ray lasers toward higher intensity, shorter pulse duration, shorter wavelength, and particularly much higher repetition rate with much less pumping laser energy [3,4]. These accomplishments were made by the use of high-repetition-rate ultrashort laser pulses produced from a chirped-pulse amplification laser system [5], and the implementation of the transient-collisional-excitation x-ray laser scheme [6] using multipulse configuration and traveling-wave pumping [7–15].

Until recently, transverse pumping geometries were used for transient-collisional-excitation solid-target x-ray lasers [7,11,13], in which the laser pulses are incident in the normal direction and thus the laser energy is absorbed over a wide region. This leads to high lasing threshold and low conversion efficiency. Great improvement in efficiency as well as x-ray beam divergence can be achieved by methods that can provide transverse energy confinement over a long gain column. This has been accomplished in two reported high-efficiency pumping schemes. One is a longitudinal pumping scheme with which Ni-like Mo x-ray lasing at 18.9 nm was demonstrated [16]. A total pump energy of 150 mJ was used and a x-ray beam of low divergence was produced. However, the plasma gradient deflects the longitudinal pump pulse away from the optimal gain region, and consequently limits the gain severely. The effect may prevent the laser from reaching saturation. The other is a grazing-incidence pumping scheme with which saturated lasing of the same line was demonstrated at subjoule pump energies [17,18].

In the past, understanding of the underlying processes for x-ray lasers was mostly deduced from the comparison between the characteristics of the x-ray pulses, such as gain and refraction, and numerical simulations [19–22]. Limited by the low repetition rate and shot-to-shot stability, diagnosis of intermediate plasma parameters, in particular plasma density gradient and electron temperature, have rarely been reported. Recently, Tommasini *et al.* reported the measurement of electron density distribution of the plasma produced by a line-focused laser pulse by using probing transmission interferometry [23], but the method cannot be used for *in situ* diagnosis (cannot be applied during the experiment of x-ray lasers). For the following reasons, *in situ* diagnosis of plasma density and temperature distribution is important for the development of x-ray lasers. (1) It enables direct comparison with the intermediate results of simulations, thereby direct examination of the hydrodynamic part of the simulation code. (2) From the density profile of the preformed plasma, the optimal incident position of the pump pulse in the longitudinal pumping scheme or the optimal incidence angle of the line-focused pump pulse in the grazing-incidence pumping scheme can be determined. This provides a step-by-step procedure to optimize the parameters of the plasma-forming pulse, the ionizing pulse, and the excitation pulse separately to attain maximum efficiency. (3) In the case of using multiple pulses to control the preformed plasma, such diagnosis is crucial for observing the creation and evolution of the plasma density profile. The information is essential for effective control of the lasing condition. (4) It reveals why some laser-target properties have been found to have critical influence on x-ray lasing, such as preionization by laser pedestal [24] and target surface roughness [25]. (5) It provides *in situ* examination and optimization of spatial overlap and timing between the pumping laser pulses.

In this paper, we report the use of longitudinal probing deflectometry and reflective interferometry to characterize the spatial and temporal distribution of the line-shaped preformed plasma fabricated for the development of solid-target x-ray laser of various pumping geometries. With the longitu-

1539-3755/2005/72(2)/026407(7)/$23.00

dinal probing deflectometry, time-resolved plasma density distribution and electron temperature in the target normal direction were resolved. The experimental data are compared with numerical simulation based on a modified version of the 1.5-D hydrodynamic and atomic physics code EHYBRID [26]. With the reflective interferometry, we show that the temporal and spatial overlap of laser pulses, the effect of laser contrast, line-focus size, target positioning, the influence of the target surface roughness, and the ionization threshold intensity of the targets can be measured *in situ*. Furthermore, we utilized these measured diagnostic data to study the effects of plasma-forming pulses in an ignitor-heater configuration. The goal is to produce optimal plasma density distributions for various pumping schemes with least laser energy. The effect of the ignitor-heater scheme on Mo, Ti, and Fe targets were individually characterized, and it was found that the scheme is most effective to Mo targets.

II. WORKING PRINCIPLES OF THE METHODS

In the longitudinal probing deflectometry a probe pulse is incident in the longitudinal direction (along the axis of the line-shaped plasma). The probe beam is deflected due to the transverse electron density gradient when passing through the plasma, and the transverse shift and the intensity of the probe beam at the end of the plasma are recorded by an imaging system. By varying the incident position transversely, plasma density and temperature distribution in the normal direction of the target can be retrieved. With varying the delay of the probe pulse with respect to the plasma-forming pulses, time evolution of the electron density and temperature distribution can be measured, and the effects of the ignitor-heater scheme on the electron density evolution can be studied. Furthermore, the plasma plume angle can also be obtained by measuring the plasma density distribution in the target normal direction at various vertical (perpendicular to the target normal and the axis of line-shaped plasma) positions.

The propagation of a probe beam in a plasma with a density gradient transverse to the beam propagation direction can be described by the ray-tracing equation [27]. Under the paraxial approximation and the conditions that the dominant component of density gradient is in the transverse direction and the refractive index remains close to unity, the ray-tracing equation can be simplified to [28]

$$\frac{d^2r}{dx^2} = \frac{\partial n}{\partial x}, \tag{1}$$

where r is the distance of the ray from the target surface and x is the coordinate perpendicular to the target surface. The electron density distribution may be retrieved with two different models. In the first model it is assumed that $\partial n/\partial x$ encountered by the probe beam in its entire path inside the plasma is constant. In this case the offset of the probe beam x_s at the exit is linked to the local density gradient by

$$x_s = \frac{1}{2}\frac{\partial n}{\partial x}L^2, \tag{2}$$

where L is the length of the plasma column. The plasma density distribution can be reconstructed from the distribution of density gradient. In the second model an exponential electron density profile is assumed, i.e.,

$$n_e(x) = n_0 \exp\left(-\frac{x}{x_0}\right). \tag{3}$$

In this case the two unknown parameters can be obtained by fitting the measured probe beam offset data to the equation [28]

$$x_s = x_0 \ln(\cosh^2\{(L/2x_0)[n_0 \exp(-x/x_0)/N_c]^{1/2}\}), \tag{4}$$

where N_c is the critical electron density for the laser wavelength and x_0 is the plasma density scale length. Once the plasma density distribution is retrieved, ray-tracing simulation can be used to calculate the probe beam offset for various incident positions. By comparing the simulated offset data with the measured data, the errors of the models can be estimated and which fits better for the experimental condition can be determined. If necessary, the second model can be extended to the superposition of two exponential distributions.

The absorption of the weak probe beam is dominant by inverse bremsstrahlung absorption, and the absorption coefficient can be written as [29]

$$\alpha = \frac{q_e^6 Z n_e^2 \ln \Lambda}{3c\omega^2 \sqrt{1 - \frac{\omega_p^2}{\omega^2}}(2\pi\varepsilon_0^2 m_e k_b T_e)^{3/2}},$$

where q_e is the electron charge, Z is the ionization stage, Λ is the Coulomb logarithm, c is the light speed, ω_p is the plasma frequency, ω is the laser frequency, m_e is the electron mass, n_e is the electron density, and T_e is the electron temperature. When the electron density and laser absorption are retrieved from experimental data, the plasma electron temperature can be obtained if the ionization stage is known. The ionization stage can be obtained from the EHYBRID simulation, or estimated by correlating this absorption measurement with the plasma expansion velocity deduced from the time-resolved measurement of the plasma density distribution.

Reflective interferometry is utilized in this experiment to find out the two-dimensional distribution of the plasma on the target surface. The measurement was carried out with a Mach-Zehnder interferometer. This diagnostic method can be used to monitor the evolution of the plasma spatial distribution, but not to quantitatively measure the plasma density and temperature distribution because of the strong absorption and refraction of the transverse probe beam and the unknown shift of the critical density layer.

III. EXPERIMENTAL SETUP

The laser used in the experiments is a 10-TW, 55-fs, 810-nm, and 10-Hz Ti:sapphire laser system based on the

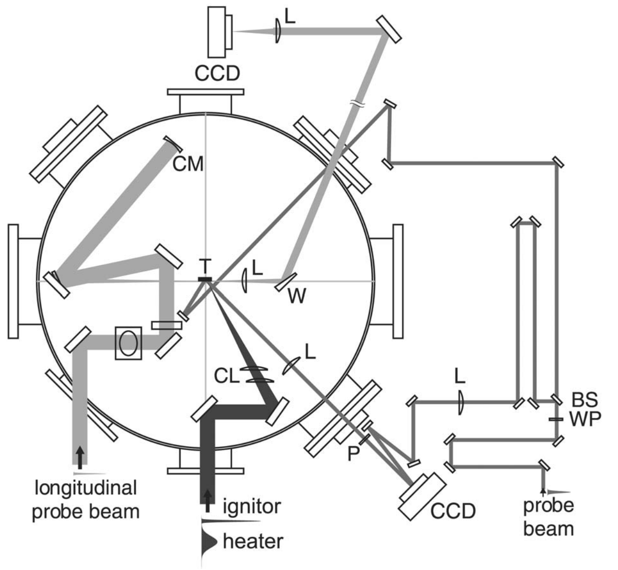

FIG. 1. Experimental layout. The acronyms represent T: target, CL: cylindrical lens, CM: concave mirror, W: wedge, WP: half-wave plate, P: linear polarizer, BS: beamsplitter, L: lens, and CCD: charge-coupled device.

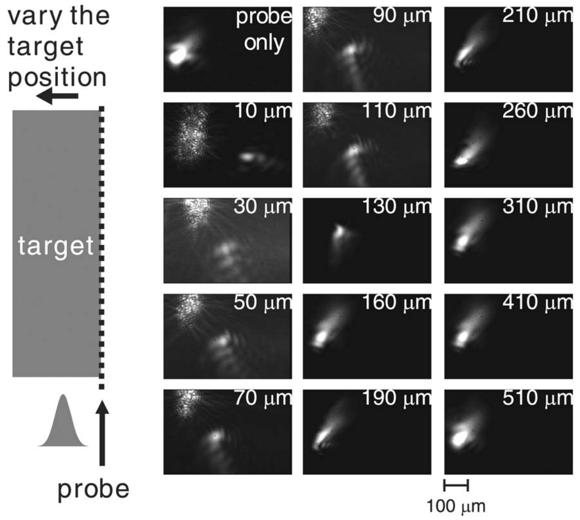

FIG. 2. Images of the longitudinal probe beam at the exit plane of the target for various incident positions relative to the target surface for 57-mJ ignitor, 240-mJ heater, 300-ps ignitor-heater separation, and 3-ns probe delay with respect to the peak of the heater. The schematic drawing shows the definition of zero position.

chirped-pulse amplification technique [30]. The temporal contrast of the compressed laser pulse was $>10^7$ at -10 ns, $>10^6$ at -50 ps, and $>10^4$ at -1 ps. The experimental setup is shown in Fig. 1. Two laser pulses, referred to as the ignitor and the heater, were used to produce the plasma, and two probe pulses were used for longitudinal probing deflectometry and transverse reflective interferometry, respectively. The s-polarized ignitor pulse was 55 fs in duration with a maximum energy of 57 mJ. The p-polarized heater pulse was 80 ps in duration with a maximum energy of 240 mJ. After being combined by a thin-film polarizer, these two beams propagated collinearly and were focused by two orthogonal cylindrical lenses ($f=200$ and 300 mm), producing a line focus of 2-mm length in full width at half maximum (FWHM) and 40-μm width FWHM on the solid target surface from near the target normal direction. The longitudinal probe beam with 55-fs duration and 40-μJ energy was focused by a concave mirror of 1-m focal length to a focal spot size of 25 μm FWHM (the corresponding Rayleigh range is 3 mm) and propagated parallel to the target surface in the direction of the axis of the line-shaped plasma. The beam position at the exit plane of the plasma was measured by relay-imaging with two spherical lenses ($f=75$ mm) and a 10× objective lens onto a charge-coupled device (CCD) camera. The energy of the longitudinal probe was set low to avoid absorption due to mechanisms other than the inverse bremsstrahlung absorption. The transverse probe beam with 55-fs duration, 2-mJ energy, and 10-mm diameter was split into two beams. The first one was incident onto the target surface at 45° in the horizontal plane. The reflected beam was then recombined with the second beam and imaged with $f=500$ mm lenses to form an interferogram (Mach-Zehnder interferometer) on a CCD camera. Linear polarizers with a contrast ratio of 10^4 were used before the CCD camera to eliminate contamination from the scattered p-polarized heater pulse to the s-polarized probe pulse that produced the interferogram.

Targets used for the measurement included polished Mo, Ti, and Fe bars, and 4-μm-thick Mo coated on Si wafer. All targets were cut to 2 mm in width to produce a 2-mm-long line-shaped plasma. For coated target the target was moved in the vertical direction after each shot to provide a fresh surface for plasma production. However, for polished target the target was moved after five shots since the results for the first five shots on the same target position were found to be almost identical. The experiment was conducted inside a vacuum chamber pumped down to <0.1 Pa. All the data points in the figures represent the average of five laser shots.

IV. EXPERIMENTAL RESULTS

For all the measurements with longitudinal probing deflectometry the zero position (target surface) was determined by the position where the probe beam was blocked by the target. However, this method has an error as large as 30 μm due to the longitudinal probe spot size, beam pointing fluctuation, and target alignment. The comparison with the simulation results shows that if the zero position was set to be at 10 μm toward the target from the position at which the probe is just blocked by the target, the retrieved electron density profile will match best with that of the simulation. Therefore, the zero position in all the figures are determined in this way. Figure 2 shows the images of the longitudinal probe beam at the exit plane of the target for various incident positions relative to the target surface for 57-mJ ignitor, 240-mJ heater, 300-ps ignitor-heater separation, and 3-ns probe delay with respect to the peak of the heater. The variation of the incident position of the longitudinal probe relative to the target surface was done by translating the target in the target normal direction. The line-focus profiles of the ignitor

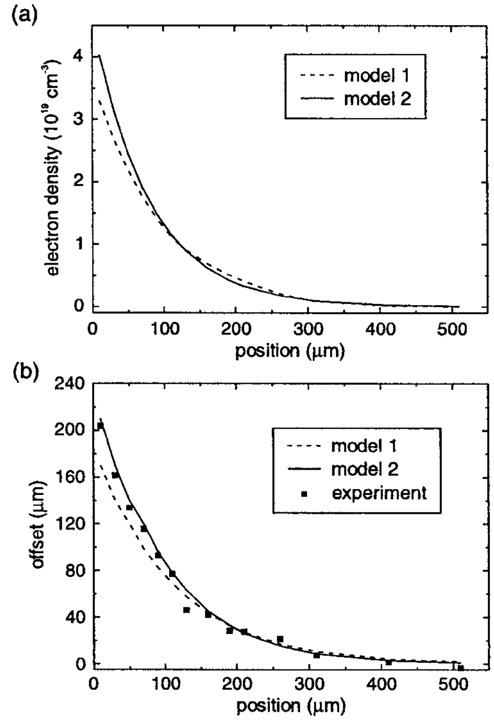

FIG. 3. Electron density distributions retrieved using the two models for the data shown in Fig. 2, (a) and the comparison between the measured probe offset (solid square) and the simulated probe offsets (dash line: model 1, solid line: model 2) based on the two retrieved traces (b).

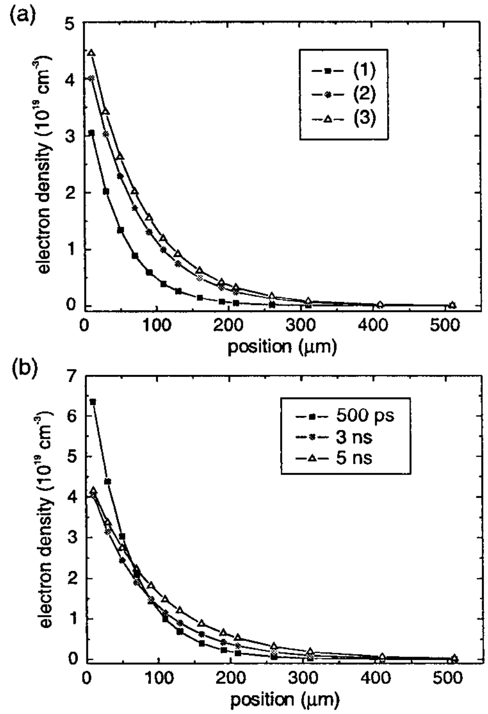

FIG. 4. (a) Electron density distributions for Mo bar with various ignitor-heater energy combinations: (1) 240-mJ heater only, (2) 20-mJ ignitor+220-mJ heater, and (3) 40-mJ ignitor+200-mJ heater. The ignitor-heater separation was 300 ps and the probe delay was 3 ns with respect to the heater. (b) Electron density distributions for Mo bar with various probe delays. The energies of the ignitor and heater were 57 and 240 mJ, respectively, and the ignitor-heater separation was 300 ps.

and the heater on the target surface did not vary significantly as the target was translated because of the long Rayleigh range. The same measurement can be done by fixing the target position and translating the steering mirror of the longitudinal probe. From the measured transverse offset of the longitudinal probe beam in the images, the electron density distribution was retrieved with the methods described in the previous section. Figure 3(a) shows the electron density distributions retrieved from Fig. 2 with the constant gradient model (model 1) and the exponential profile model (model 2), respectively. The electron density distributions obtained with these two models are very close to each other in the low electron density region, but show deviation in the high density region. Figure 3(b) shows the comparison between the measured probe offset and the probe offset calculated with ray-tracing simulation based on the two retrieved electron density distributions. The exponential profile model matches very well with the measurement for the entire plasma region, therefore this model was adopted for all the data presented in this paper. Since the probe offset is linearly proportional to the density gradient, the systematic error in the absolute value of the electron density deduced is estimated to be 6.5% at 50 μm (higher-density region) and 1.3% at 310 μm (lower-density region).

Figure 4(a) shows the electron density distribution for Mo bar with various ignitor-heater energy combinations and 3-ns probe delay with respect to the heater. Figure 4(b) shows the electron density distribution for Mo bar with various probe delays. The energies of the ignitor and heater were 57 and 240 mJ, respectively, and the ignitor-heater separation was 300 ps. The same measurements were done for Ti and Fe bars, as shown in Figs. 5 and 6. As shown, by splitting a small amount of energy from the heater to serve as the ignitor, a plasma of higher density and larger scale length can be produced for Mo. Diverting more energy to the ignitor does not create a larger effect. However, for Ti and Fe the diversion of some energy to the ignitor does not show significant enhancement. The enhancement by the ignitor-heater scheme may be ascribed to the increased amount of seed electrons produced by the ignitor that leads to an increased growth rate of collisional ionization and inverse bremsstrahlung heating during the heater, or by the change of the initial plasma density slope encountered by the heater. To understand the cause for the stronger effect on Mo bars than on Ti and Fe, the ionization threshold intensities for these targets were measured by using the reflective interferometry to observe the appearance of plasma with varying ignitor energy. The threshold were roughly 4.8×10^{13}, 2.0×10^{13}, and 2.0×10^{13} W/cm^2 for Mo, Ti, and Fe, respectively. The experimental results indicate that an ignitor is more beneficial for Mo compared to Ti and Fe because of the higher ionization threshold intensity. From the dc tunneling ionization theory by Augst *et al.* [31], the ionization threshold intensities of Mo, Ti, and Fe targets are 1.0×10^{13} (I_p=7.1 eV), 8.6×10^{12} (I_p=6.82 eV), and 1.5×10^{13} W/cm^2 (I_p=7.87 eV), respectively. This is not in agreement with our measurement.

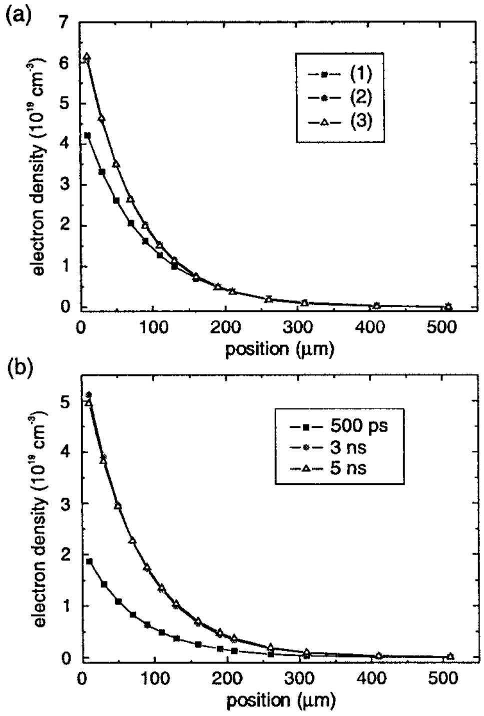

FIG. 5. (a) Electron density distributions for Ti bar with various ignitor-heater energy combinations: (1) 240-mJ heater only, (2) 20 -mJ ignitor+220-mJ heater, and (3) 40-mJ ignitor+200-mJ heater. The ignitor-heater separation was 300 ps and the probe delay was 3 ns with respect to the heater. (b) Electron density distributions for Ti bar with various probe delays. The energies of the ignitor and heater were 57 and 240 mJ, respectively, and the ignitor-heater separation was 300 ps.

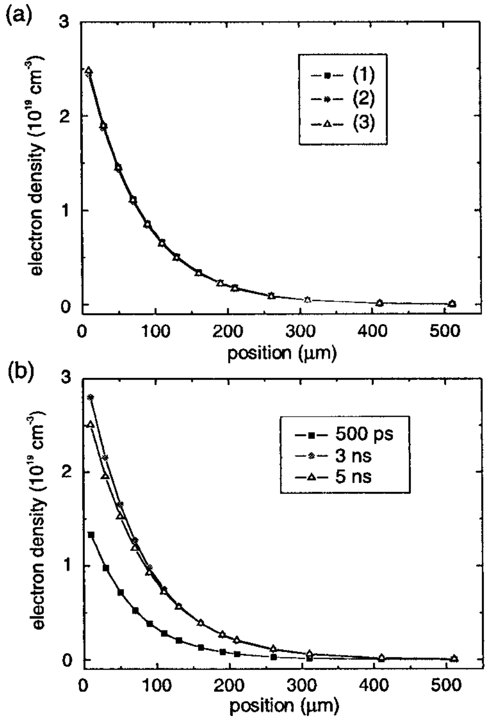

FIG. 6. (a) Electron density distributions for Fe bar with various ignitor-heater energy combinations: (1) 240-mJ heater only, (2) 20 -mJ ignitor+220-mJ heater, and (3) 40-mJ ignitor+200-mJ heater. The ignitor-heater separation was 300 ps and the probe delay was 3 ns with respect to the heater. (b) Electron density distributions for Fe bar with various probe delays. The energies of the ignitor and heater were 57 and 240 mJ, respectively, and the ignitor-heater separation was 300 ps.

Recently, Smits *et al.* [32] reported that the calculation of ionization threshold intensity should include the dynamic polarization or screening effects from other electrons in the atom, in particular for transition metal atoms. These effects lead to a dramatic suppression of the ionization in comparison to that calculated under the single active electron approximation. As a result, the relative magnitude of ionization threshold intensity for these three targets may be changed to that shown in our measurement.

Figure 7 shows the electron density distributions from the experimental measurement and the EHYBRID simulation for the Mo target with 240-mJ heater only and 20-mJ ignitor +220-mJ heater, respectively. The ignitor-heater separation was 300 ps and the probe delay was 3 ns. For the case of using the heater only the electron density distribution from simulation is similar to that measured in the experiment except for the region very close to the target surface. However, for the case of ignitor-heater scheme the simulation results are not consistent with the measurement. This may be because the simulation code considers only inverse bremsstrahlung heating and collisional ionization so that the significant influence of the ignitor through optical-field ionization and other heating mechanisms are not taken into account.

Figure 8 shows the distribution of average ionization stage and electron temperature from the simulation for the Mo target with 57-mJ ignitor, 240-mJ heater, 300-ps ignitor-heater separation, and 3-ns probe delay. It shows that the average ionization stage is 6 in the region of 100–150 μm from the target surface. From this data and the measured electron density, the electron temperature in this region can be retrieved by using the formula of inverse bremsstrahlung absorption. The retrieved electron temperature, shown in Fig. 8, shows reasonable consistency with the simulation results. If the heating by the ignitor is raised artificially in the simulation, the measured temperature can match even better with

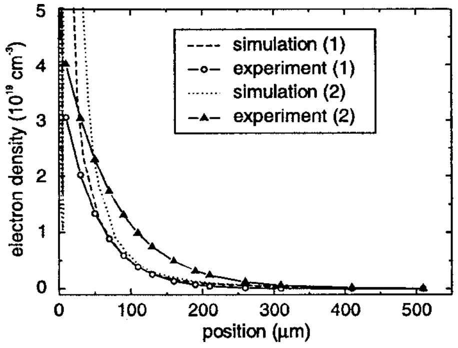

FIG. 7. Electron density distributions from the experimental measurement and the EHYBRID simulation for Mo target with (1) 240-mJ heater only and (2) 20-mJ ignitor+220-mJ heater, respectively. The ignitor-heater separation was 300 ps and the probe delay was 3 ns.

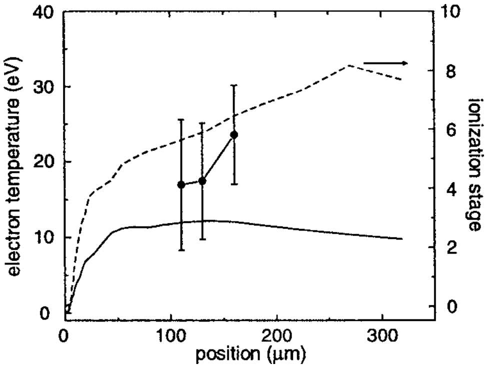

FIG. 8. Distribution of average ionization stage (dash line) and electron temperature (solid line) from the simulation for Mo target with 57-mJ ignitor, 240-mJ heater, 300-ps ignitor-heater separation, and 3-ns probe delay. With the average ionization stage obtained from simulation and the measured electron density the electron temperature was retrieved from the absorption data and plotted for comparison (solid circle).

the simulation result. This again indicates that under our experimental conditions there are additional effects of heating by the ignitor not included in the EHYBRID simulation, in agreement with the comparison of electron density distribution between experimental measurement and simulation. The cause for missing the heating effects may be because the EHYBRID simulation was not originally designed for simulating pump pulses shorter than 200 fs. Note that in this experiment the transverse ignitor and heater pulses are used only to preform a plasma with a density distribution suitable for x-ray lasers, not to produce the lasing ion species.

In this experiment we can only retrieve the electron temperature in the region of 100–150 μm. This is because the absorption measurement is only reliable in this region, since in the higher density region the probe intensity is reduced also by deflection out of the imaging system and in the lower density region the absorption is too small to be accurately measured. The electron temperature can also be estimated from the expansion velocity of the plasma. In Fig. 4(b), the layer with 1×10^{19}-cm^{-3} density moves 20 μm from 0.5 to 3 ns. Using the formula of sound speed and the ionization stage of 6, the electron temperature is calculated to be 10 eV. From the expansion of the layer of 5×10^{18}-cm^{-3} density, the temperature is calculated to be 28 eV. This range of electron temperature is consistent with the measurement based on absorption of the longitudinal probe pulse.

By measuring the electron density distribution in the target normal direction at various vertical positions, the two-dimensional plasma density distribution perpendicular to the axis of line-shape plasma can be measured. The result is shown in Fig. 9 for Mo-coated targets under the same condition as in Fig. 8. The electron density distribution consists of two components. The first one with a larger transverse distribution has a smaller density scale length. The second one with a smaller transverse distribution has much larger density and density scale length than the first one. We have identified that the first component was produced by the ignitor alone and the second component was produced together by the ignitor and the heater.

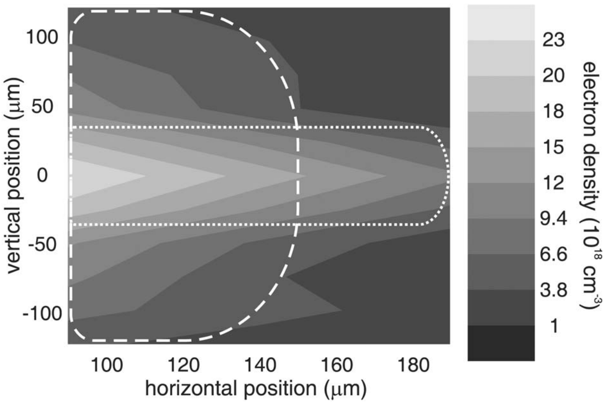

FIG. 9. Two-dimensional plasma density distribution perpendicular to the axis of line-shaped plasma for Mo-coated targets with 57-mJ ignitor, 240-mJ heater, 300-ps ignitor-heater separation, and 3-ns probe delay. The dash line indicates the first component of smaller scale length and the dot line indicates the second one of larger scale length.

Another important factor for efficient x-ray lasing is the surface roughness. Tommasini *et al.* reported that the slope efficiency of x-ray lasing can be improved by a factor of 4 when the surface roughness is changed from 0.7 to 0.07 μm [25]. If the surface roughness is large, nonuniformity in the plasma will lead to disruption of x-ray amplification, reducing the lasing efficiency. Figures 10(a)–10(d) shows the images of reflective interferometry of Mo-coated targets and polished Mo bars before and after the ignitor-heater pulses

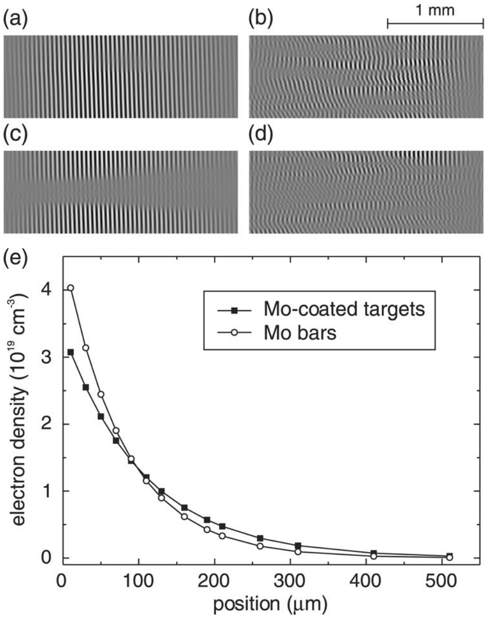

FIG. 10. Reflective interferograms of Mo-coated targets and polished Mo bars before, (a) and (b), and after, (c) and (d), the ignitor-heater pulses for 57-mJ ignitor, 240-mJ heater, 300-ps ignitor-heater separation, and 3-ns probe delay. The intensity of the interferograms are uniformized by a numerical method to make the fringes clearly observable. The electron density distributions in the target normal direction measured with longitudinal deflectometry for these two targets are shown in (e).

for 57-mJ ignitor, 240-mJ heater, 300-ps ignitor-heater separation, and 3-ns probe delay. The fringe shift distribution shows that a coated target has a much better flatness than a polished target, and the large roughness of polished targets remains imprinted on the produced plasma even after the plasma has expanded for several hundred micrometers. Figure 10(e) shows the electron density distributions in the target normal direction measured with longitudinal deflectometry for these two targets. The plasma produced from Mo-coated targets shows only a slight difference compared to that from Mo bars. Therefore, the disadvantage of using a polished target compared to a coated target lies mainly in the nonuniformity of plasma along the x-ray lasing direction instead of the plasma density scale length in the target normal direction. Reflective interferometry can also be used to measure the distribution of the produced plasma on the target surface to get a good estimation of gain length, to examine the spatial and temporal overlaps between the line foci of the laser pulses, and to position the exit edge of the target right at the end of the uniform gain region so that the absorption of the x-ray output by the colder plasma can be avoided. These are also important factors that affect x-ray lasing efficiency.

V. CONCLUSION

In summary, by using longitudinal probing deflectometry and transverse reflective interferometry together, we have shown that the plasma electron density and electron temperature distributions can be characterized for the development of solid-target x-ray lasers. In particular, effects of the plasma-forming pulses in the ignitor-heater scheme can be studied systematically. Effects of surface roughness, the laser pedestal, and spatial-temporal overlap between the laser pulses can also be examined. All these issues are crucial to achieving high pumping efficiency and high-quality x-ray output. With these *in situ* diagnostic tools it becomes possible to examine the lasing condition in detail and optimize it step by step. In other words, through measurements of the intermediate plasma parameters, one may be able to narrow the gap between physics and engineering in the development of x-ray lasers.

---

[1] D. L. Matthews *et al.*, Phys. Rev. Lett. **54**, 110 (1985).
[2] M. D. Rosen *et al.*, Phys. Rev. Lett. **54**, 106 (1985).
[3] J. J. Rocca, Rev. Sci. Instrum. **70**, 3799 (1999).
[4] H. Daido, Rep. Prog. Phys. **65**, 1513 (2002).
[5] D. Strickland and G. Mourou, Opt. Commun. **56**, 219 (1985).
[6] Yu. V. Afanasiev and V. N. Shlyaptsev, Sov. J. Quantum Electron. **19**, 1606 (1989).
[7] P. V. Nickles, V. N. Shlyaptsev, M. Kalachnikov, M. Schnurer, I. Will, and W. Sandner, Phys. Rev. Lett. **78**, 2748 (1997).
[8] J. Dunn, A. L. Osterheld, R. Shepherd, W. E. White, V. N. Shlyaptsev, and R. E. Stewart, Phys. Rev. Lett. **80**, 2825 (1998).
[9] M. P. Kalachnikov *et al.*, Phys. Rev. A **57**, 4778 (1998).
[10] P. J. Warwick *et al.*, J. Opt. Soc. Am. B **15**, 1808 (1998).
[11] J. Dunn, Y. Li, A. L. Osterheld, J. Nilsen, J. R. Hunter, and V. N. Shlyaptsev, Phys. Rev. Lett. **84**, 4834 (2000).
[12] A. Klisnick *et al.*, J. Opt. Soc. Am. B **17**, 1093 (2000).
[13] R. E. King *et al.*, Phys. Rev. A **64**, 053810 (2001).
[14] T. Kawachi *et al.*, Phys. Rev. A **66**, 033815 (2002).
[15] Y. Li *et al.*, J. Opt. Soc. Am. B **17**, 1098 (2000).
[16] T. Ozaki, R. A. Ganeev, A. Ishizawa, T. Kanai, and H. Kuroda, Phys. Rev. Lett. **89**, 253902 (2002).
[17] R. Keenan, J. Dunn, P. K. Patel, D. F. Price, R. F. Smith, and V. N. Shlyaptsev, Phys. Rev. Lett. **94**, 103901 (2005).
[18] B. M. Luther *et al.*, Opt. Lett. **30**, 165 (2005).
[19] A. Behjat *et al.*, Opt. Commun. **135**, 49 (1997).
[20] J. Nilsen, Y. Li, and J. Dunn, J. Opt. Soc. Am. B **17**, 1084 (2000); J. Nilsen, J. Dunn, R. F. Smith, and T. W. Barbee, Jr., *ibid.* **20**, 191 (2003).
[21] X. Lu, Y. J. Li, Y. Cang, K. Li, and J. Zhang, Phys. Rev. A **67**, 013810 (2003).
[22] J.-Y. Lin, Jpn. J. Appl. Phys., Part 1 **40**, 4A-84 (2001).
[23] R. Tommasini, K. Eidmann, T. Kawachi, and E. E. Fill, Phys. Rev. E **69**, 066404 (2004).
[24] K. A. Janulewicz, A. Lucianetti, G. Priebe, W. Sander, and P. V. Nickles, Phys. Rev. A **68**, 051802(R) (2003).
[25] R. Tommasini, F. Löwenthal, and J. E. Balmer, Phys. Rev. A **59**, 1577 (1999).
[26] G. J. Pert, J. Fluid Mech. **131**, 401 (1983).
[27] M. Born and E. Wolf, *Principles of Optics* (Pergamon Press, 1980).
[28] E. E. Fill, J. Opt. Soc. Am. B **14**, 1505 (1997).
[29] T. W. Johnston and J. M. Dawson, Phys. Fluids **16**, 722 (1973).
[30] H. H. Chu *et al.*, Appl. Phys. B: Lasers Opt. **79**, 193 (2004).
[31] S. Augst, D. Strickland, D. D. Meyerhofer, S. L. Chin, and J. H. Eberly, Phys. Rev. Lett. **63**, 2212 (1989).
[32] M. Smits, C. A. de Lange, A. Stolow, and D. M. Rayner, Phys. Rev. Lett. **93**, 213003 (2004).